The compression of a heavy floating elastic film

Etienne Jambon-Puillet[a], Dominic Vella[a,b] and Suzie Protière*[a]

Received Xth XXXXXXXXXX 20XX, Accepted Xth XXXXXXXXX 20XX
First published on the web Xth XXXXXXXXXX 200X
DOI: 10.1039/b000000x

We study the effect of film density on the uniaxial compression of thin elastic films at a liquid–fluid interface. Using a combination of experiments and theory, we show that dense films first wrinkle and then fold as the compression is increased, similarly to what has been reported when the film density is neglected. However, we highlight the changes in the shape of the fold induced by the film's own weight and extend the model of Diamant and Witten [*Phys. Rev. Lett.*, 2011, **107**, 164302] to understand these changes. In particular, we suggest that it is the weight of the film that breaks the up-down symmetry apparent from previous models, but elusive experimentally. We then compress the film beyond the point of self-contact and observe a new behaviour dependent on the film density: the single fold that forms after wrinkling transitions into a closed loop after self-contact, encapsulating a cylindrical droplet of the upper fluid. The encapsulated drop either causes the loop to bend upward or to sink deeper as compression is increased, depending on the relative buoyancy of the drop-film combination. We propose a model to qualitatively explain this behaviour. Finally, we discuss the relevance of the different buckling modes predicted in previous theoretical studies and highlight the important role of surface tension in the shape of the fold that is observed from the side — an aspect that is usually neglected in theoretical analyses.

1 Introduction

The formation of wrinkles and their localization into folds is observed when a layered material is progressively compressed. As such, they occur in a variety of systems at different scales in Nature from the folding of geological strata[1] to the morphogenesis of biological tissues such as the cerebral cortex[2–4] or fingerprints[5] as well as in the growth of biofilms[6]. Just as nature uses these mechanical instabilities to generate intricate patterns, wrinkling instabilities are also finding a number of technological applications from flexible electronic devices[7,8] to controlled patterned surfaces[9,10] that have improved light harvesting efficiency[11] or surface hydrophobicity[12]. Because of this ubiquity and the renewed interest in taking control of elastic instability, the deformation of layered elastic materials has been the object of renewed interest recently, with a number of fundamental studies in the past decade[13–17].

The simplest example of elastic instability is the classic Euler buckling[18,19] in which a compressed beam buckles over its entire length. To use elastic instability for pattern formation usually requires the selection of a length scale other than the system size, however. Perhaps the simplest example of such a system is provided by an elastic film (of bending stiffness per unit width B) floating on a liquid of density ρ and subject to an axial compression. This system quickly forms wrinkles with a wavelength $\lambda \sim (B/\rho g)^{1/4}$ — a result that expresses the compromise between the bending rigidity of the film (which prefers large-amplitude wrinkles) and the weight of the liquid (g being the gravitational acceleration), which prefers many small-amplitude wrinkles[20–23]. This wrinkling instability can also be observed in other types of floating materials such as thin layers of nanoparticles[24], surfactants[25,26] or particle rafts[27]. However, at some point most of these wrinkles begin to shrink with a very small number growing to form much larger 'folds'; although other options (such as delamination[28]) exist, folds are more generically observed and so we focus on them in this paper.

The nature of the wrinkle-to-fold transition in this system has been somewhat controversial: it was initially suggested (on the basis of experiments) that folds form at a critical compression. Several numerical and analytical works have studied the wrinkle-to-fold transition in idealized situations (in which the elastic film is infinitely long and weightless[29–32]) and have shown that in these scenarios the transition is not sharp: i.e. folds emerge continuously from the wrinkled state. Recently, a more realistic model (incorporating the finite length of the film) demonstrated that this transition emerges at a finite compression making a second-order transition[33,34]. Despite the amount of work on the wrinkle-to-fold transition, several questions remain unanswered. For example, existing models suggest that downwards and upwards folds should be equally

---

† Electronic Supplementary Information (ESI) available: [details of any supplementary information available should be included here]. See DOI: 10.1039/b000000x/

[a] *Institut Jean le Rond d'Alembert, UPMC Paris 6, CNRS UMR 7190, 4 Pl Jussieu, 75005, Paris, France. Email: protiere@ida.upmc.fr*

[b] *Mathematical Institute, Andrew Wiles Building, University of Oxford, Woodstock Rd, Oxford, OX2 6GG, UK*

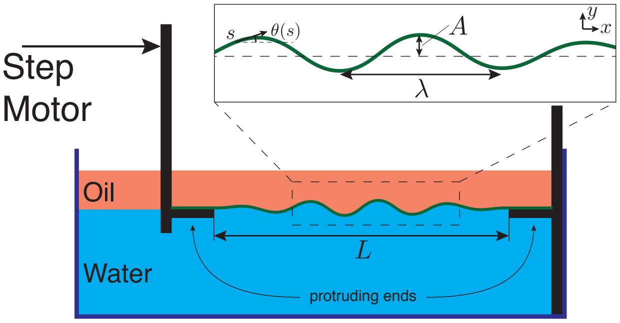

Fig. 1 Schematic of the experimental setup defining the length L between the boundaries, the wrinkle wavelength λ and the wrinkle amplitude A as well as the Cartesian and intrinsic coordinates used in the model: (x,y) and (s,θ).

favourable, while experiments report exclusively downward folds. Moreover, what happens beyond the transition between these two states has not been described experimentally but only via numerical simulations[35] with the weight of the film discussed in scaling terms. In the first part of this paper we investigate the effect of the film weight on the wrinkle-to-fold transition while in the second part we focus on the evolution of the fold upon further compression. We observe that the fold becomes a closed loop after self-contact, encapsulating a volume of the upper fluid. As the applied compression is increased, we observe that the fold either sinks deeper without limit or eventually bends upward, depending on the relative buoyancy of the drop-film combination. We predict the regime diagram for this behaviour theoretically.

2 Experimental section

Elastic film production: Thin elastic films are produced by spincoating vinylpolysiloxane VPS (elite double 32, `Zhermack`) of base density $\rho_{VPS} = 1.20\,\mathrm{g\,cm^{-3}}$. To produce films of various densities, we add iron powder (97%, -325 mesh, `Sigma Aldricht`) $\rho_{Fe} = 7.87\,\mathrm{g\,cm^{-3}}$ to the non cross-linked polymer. This allows us to work with films of densities $\rho_s = 1.2 - 2.6\,\mathrm{g\,cm^{-3}}$ (see table, ESI†). The spincoated polymer/iron mixture viscosity changes with the iron powder concentration so that at a fixed rotation speed the film thickness, t, obtained varies. We adjust the rotation speed to narrow the thickness range ($50\,\mu\mathrm{m} < t < 120\,\mu\mathrm{m}$). Two sets of film lengths L_0 and width W are produced: $L_0 = 90$ mm, $W = 60$ mm and $L_0 = 75$ mm, $W = 50$ mm.

Compression experiment:

The experiments are conducted in a glass tank ($12 \times 11 \times 6.5\,\mathrm{cm^3}$) with two parallel polymethylmethacrylate (PMMA) plates with horizontal protruding ends (Fig. 1). The tank is filled with tap water to a level higher than the protruding ends. The elastic film is then carefully placed at the air/water interface between the plates. The water level is then lowered (using a syringe) until the edges of the film comes into contact with the protruding ends of the PMMA plates. The film naturally adheres strongly to the PMMA achieving a clamped boundary condition at the protruding ends. The water level is adjusted with the syringe so that the film is completely flat. A light mineral oil ($\rho_o = 0.836\,\mathrm{g\,cm^{-3}}$, `Sigma Aldrich`) is then poured slowly on top of the film (so that no oil invades the lower surface of the film, in contact with water). One of the PMMA plates is mounted on two perpendicular manual translation stages for alignment in the (y,z) direction and connected to a stepper motor (`Thorlabs`) of micrometer precision. The compression is quasi-static: the stepper motor displaces the plate in small increments at a constant speed. The motor stops for 5s between each step allowing the system to relax to its equilibrium shape. The elastic film is imaged from the side and/or the top with two `Nikon` D800-E cameras mounted with macro objectives (105 mm). The images are then analysed using either `ImageJ` or `MATLAB`.

Film analysis:

We use two methods to determine the elastic films thicknesses. We weigh the films on a milligram scale: knowing the density, length and width we deduce an average thickness. We also illuminate the films with a tilted laser line. The laser deflection being a function of the height and tilting angle, height profiles are then extracted using the appropriate calibration. Both measurement techniques give similar results. In addition, the laser line allows us to check that our films are uniform: thickness variations are below the measurement standard deviation ($\pm\,10\,\mu$m) except at the edges of the film where a small ridge ($20\,\mu$m thicker) develops during the spin coating/curing. The Young's modulus E and Poisson ratio ν are determined by a tensile test on a dogbone shape using a `Shimadzu` tensile machine. For the pure VPS we find $E = 1.0$ MPa, $\nu = 0.5$ while for the VPS/iron particle mixture the Young's modulus increases up to $E = 2.9$ MPa for a dogbone of density $\rho_s = 2.5\,\mathrm{g\,cm^{-3}}$. We checked that the film Young's modulus is the same as that obtained from the test samples by measuring the deflection of the film under its own weight. By letting a small portion of the film protrude out of a clamp we were able to vary the length easily and fit the bending stiffness $B = Et^3/\left[12(1-\nu^2)\right]$. The values found through this procedure are in good agreement with the previously measured E and t. Finally the measured E and t are compatible with the direct measurement of the wrinkle wavelength λ (see table, ESI†).

3 Results

We compress an elastic film floating at an interface between two fluids and study its behaviour as we increase the imposed displacement. At zero compression, $L = L_0$, the film lies flat at the interface. As soon as we start compressing the film ($\Delta = L_0 - L > 0$), it buckles out of plane with a characteristic wavelength λ that develops along the film length (Fig. 2 (a)). This is the wrinkled state. As Δ increases, the wrinkle amplitude A initially grows uniformly (Fig. 2 (b)) until, suddenly, only one of the wrinkles continues to grow while the other wrinkles progressively vanish. The excess length of the vanished wrinkles is absorbed by the remaining structure, the fold (Fig. 2(c)). We therefore observe a clear transition between the "wrinkled state", in which the deformation is distributed throughout the film, and a "fold state", in which all the deformation is localized in a narrow region of high curvature, *i.e.*: the fold. As the compression Δ is increased beyond the wrinkle-to-fold transition, the fold continues to grow in amplitude and its curvature increases. Finally, the two opposing edges of the fold come into contact (self-contact). At this point a horizontal column of the upper fluid is encapsulated in this "teardrop" shape (Fig. 2 (d)). With further increases in compression this teardrop is forced down into the subphase and does not noticeably change shape; instead the length over which the film is in self-contact increases (Fig. 2 (e)). In this paper, we study the role of the density of the elastic film in the wrinkle-to-fold transition and its impact on the evolution of the fold as the uniaxial compression is increased to the point of self-contact and beyond.

3.1 Wrinkle-to-fold transition and fold before self-contact

In order for the fold to nucleate near the centre of the elastic film, at $L_0/2$, we ensure that the clamped edges are aligned very carefully. (The fold has to appear at least one wavelength λ away from the clamped edges to avoid any boundary effects.) The results were compared to a fold generated by applying a small pressure at the film centre before starting to compress it. For three different densities $\rho_s = 1.2,\ 1.4,\ 1.8\ \mathrm{g\,cm^{-3}}$ and two different film lengths L_0, we used images taken from the side to measure the fold amplitude A during compression up to self-contact. The data are then normalized by the wavelength λ measured experimentally (Fig. 3). For small compressions, $\Delta/\lambda \lesssim 0.3$ we observe the wrinkled state with no influence of the film weight. In this wrinkled regime, Pocivavsek *et al.*[20] found that the evolution of the wrinkle amplitude exhibits a weak dependence on the film length, which we are not able to observe in our experiments. Moreover, Rivetti and Neukirch[33] also predict that the buckling modes (symmetric/antisymmetric/non symmetric) of the film can evolve during the compression for different film lengths. We do observe two different buckling routes in our experiments and they are responsible for the two different trends in the amplitude that we observe in Fig. 3: the experi-

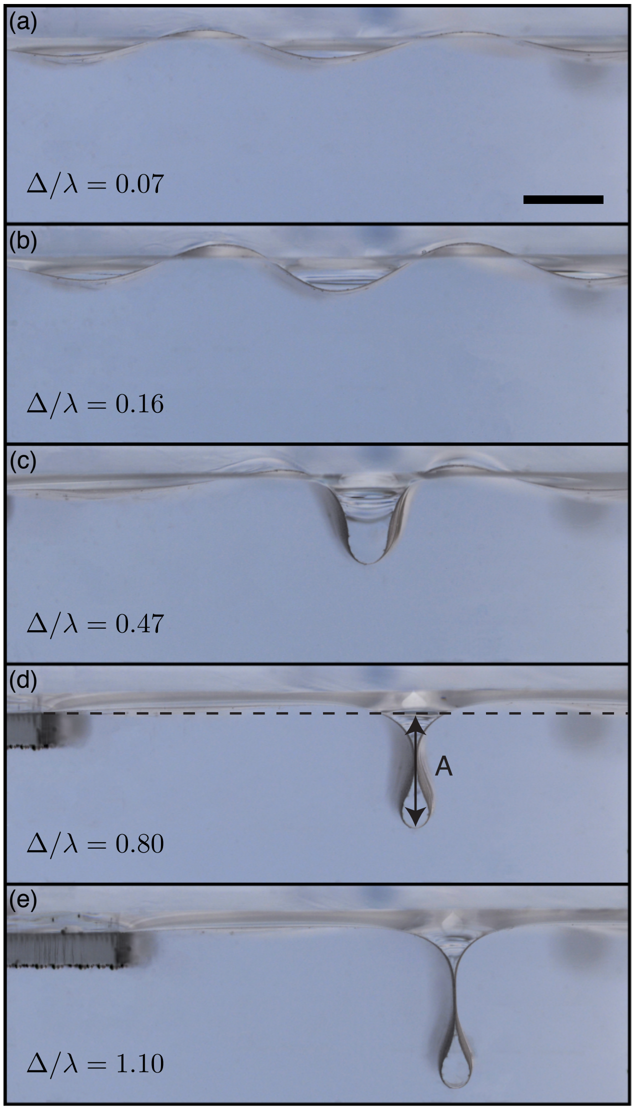

Fig. 2 Side images of an elastic film of density $\rho_s = 1.8\, g.cm^{-3}$ at an oil/water interface. Compression Δ increases from **(a)** to **(e)**, scale bar 5mm. Colours have been inverted to enhance contrast. **(a)-(b)** The film displays a quasi-periodic out of plane displacement of amplitude A and wavelength λ, referred to as the wrinkled state. **(c)** The deformation localizes in a single fold. **(d)** The fold reaches self-contact. **(e)** A column of oil is encapsulated in the fold which grows deeper towards the bottom of the tank as compression is increased.

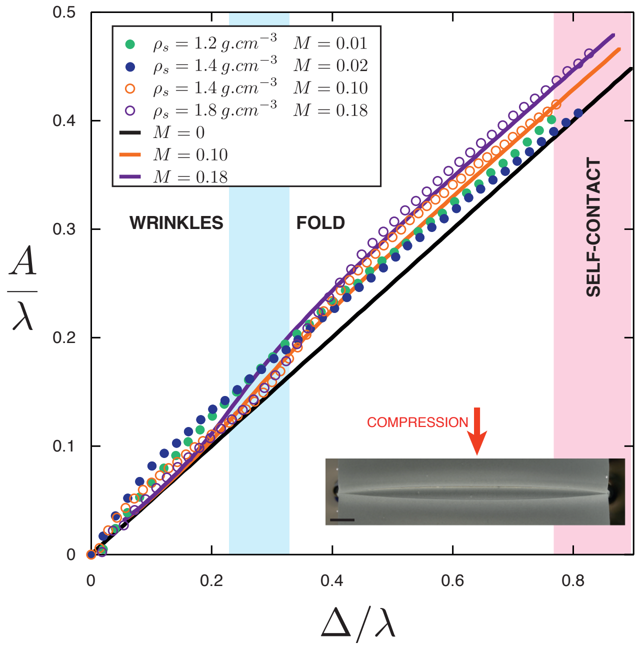

Fig. 3 Dimensionless wrinkle/fold amplitude as a function of the dimensionless compression up to self-contact. (○, ○) represent oil/water experiments, (●, ●) air/water experiments. Three film densities are presented (with different lengths/widths/thicknesses), giving rise to the four dimensionless weights presented in the legend. The black curve corresponds to the symmetric solution[29] ($M = 0$), the orange and purple curves correspond to the symmetric numerical solution of equation (4) for $M = 0.10$ and $M = 0.18$. *Inset*: Top view of the compressed film. The fold reaches self-contact at the edges of the film but is still open in the centre (see ESI†). Scale bar: 5mm.

ments at an air–water interface remain symmetric throughout the compression while the experiments at an oil–water interface start antisymmetric but switch continuously to a symmetric mode. Since the antisymmetric mode has a smaller amplitude (for a given compression) than the symmetric one, when the fold switches to the symmetric mode its amplitude increases rapidly. This results in an inflection point at $\Delta/\lambda \sim 0.3$ for experiments at an oil–water interface. However, these details are very sensitive to the experimental conditions (particularly to the clamped boundary conditions) and no quantitative comparison could be made with the predictions of Rivetti and Neukirch[33] (see ESI†). For larger compressions, $\Delta/\lambda > 0.4$, the behaviour does not depend on film length: the deformation always localizes in a downward symmetric fold with an amplitude that grows linearly with compression, as described previously[20,29].

However, as we vary the film densities we find that the amplitude of the fold increases slightly with the film mass (Fig. 3). To explain this dependence we first turn to the model developed by Diamant and Witten[29] for the nonlinear deflections of a floating elastic film. In the limit of an incompressible, weightless film of infinite length, this model has an analytical solution[29]; here we shall have to develop a numerical solution but we first outline the derivation of the governing equation for a light film, so that the appropriate modifications can be made for the film weight. We introduce the intrinsic coordinates (s,θ), where θ is the angle between the film and the horizontal axis and s is the arc-length; the film centreline is then parametrized in terms of arc-length, $[x(s), y(s)]$. The energy U of a film of bending stiffness B and width W contains contributions from bending $U_b = \frac{1}{2}BW\int_{-\infty}^{\infty}(\partial_s\theta)^2\,\mathrm{d}s$ and from the gravitational potential energy of the underlying fluid substrate U_s. In our case the gravitational energy of the upper and lower fluids $U_{l_{up}}$ and $U_{l_{low}}$, respectively are given by: $U_s = U_{l_{up}} + U_{l_{low}} = \frac{1}{2}\Delta\rho g W\int_{-\infty}^{\infty}y(s)^2\cos\theta\,\mathrm{d}s$ where the relevant density is the density difference between the two fluids $\Delta\rho = \rho_{low} - \rho_{up}$. The energy is to be minimized subject to the constraint of an imposed compression $\Delta = \int_{-\infty}^{\infty}(1-\cos\theta)\,\mathrm{d}s$. To facilitate the calculation, lengths are non-dimensionalized by $\ell_{eh} = \left[B/(\Delta\rho g)\right]^{1/4} = \lambda/(2\pi)$ and energies by WB/ℓ_{eh}. The minimization itself is discussed in detail by Diamant and Witten[29] and yields a single equation for the intrinsic angle $\theta(s)$ with the boundary conditions $\theta(\pm\infty) = \partial_s\theta(\pm\infty) = y(\pm\infty) = 0$:

$$\partial_s^4\theta + \left[\tfrac{3}{2}(\partial_s\theta)^2 + P\right]\partial_s^2\theta + \sin\theta = 0 \tag{1}$$

Here P is the Lagrange multiplier associated with the compression constraint, and corresponds physically to the dimensionless horizontal force applied on the elastic film by the compression. Equation (1) has a family of analytical solutions[29,30,32]:

$$\theta(s) = 4\arctan\left(\frac{\kappa\sin\left[k(s+\phi)\right]}{k\cosh(\kappa s)}\right)$$
$$k = \tfrac{1}{2}\sqrt{2+P}, \quad \kappa = \tfrac{1}{2}\sqrt{2-P}, \quad P = 2 - \frac{\Delta^2}{16}. \tag{2}$$

This family of solutions is parametrized by ϕ, with $0 \le k\phi \le \pi$; the value of $k\phi$ selects the symmetry of the profile[32], with $k\phi = 0$ corresponding to an even fold and $k\phi = \pi/2$ corresponding to an odd fold[29].

For the experiments presented in this paper, the weight of the film is not negligible; we must therefore supplement the bending and substrate energy with the gravitational energy of the film itself, U_g. If ρ_s is the density of the film and ρ_w the density of the lower liquid (water) then the dimensionless gravitational energy of the film is

$$U_g = M\int_{-\infty}^{\infty} y(s)\,\mathrm{d}s,$$

where

$$M = \frac{(\rho_s - \rho_w)t}{\Delta\rho\,\ell_{eh}} \tag{3}$$

is a dimensionless number that compares the weight of the film to the restoring force provided by buoyancy over the horizontal length ℓ_{eh}. Applying the energy minimization procedure described by[29] to the total energy $U = U_s + U_b + U_g$ we obtain the system of equations (see ESI† for details):

$$\partial_s^4\theta + \left[\tfrac{3}{2}\left(\partial_s\theta\right)^2 + P - My\right]\partial_s^2\theta + (1 - 2M\partial_s\theta)\sin\theta = 0$$
$$\partial_s x = \cos\theta, \quad \partial_s y = \sin\theta \tag{4}$$

using the same clamped boundary conditions as for the light film. We note that, as expected, the weightless equation (1) is recovered by setting $M = 0$.

For $M \neq 0$, we are not able to find an analytical solution of the system of equations (4); instead we obtain numerical solutions by using the `MATLAB` routine `bvp4c`, which uses a relaxation technique with the analytical solution (2) as an initial guess. We also use a simple continuation algorithm to find the solutions as parameters are varied.

Our numerical solutions suggest that the antisymmetric solution no longer exists once $M \neq 0$ (we are unable to find numerical solutions with this symmetry). Even if an antisymmetric solution of equation (4) does exist, with $M > 0$ (respectively $M < 0$), the downward (respectively upward) symmetric solution has a lower energy due to the contribution of the gravitational term U_g. (In the limit $M = 0$, all of the solutions (2) are known to have the same energy[29–32].) The weight of the film therefore lifts the degeneracy that was inferred from the analytical solution (2) but this has not been observed experimentally[20]; previously this breaking of symmetry was attributed to surface tension, but not quantified[20].

Experimentally, we do, in fact, observe antisymmetric configurations for sufficiently low compressions ($\Delta/\lambda \lesssim 0.25$); however, as the compression increases, the film always evolves to a downward symmetric configuration (see ESI†). This is in accordance with the theoretical prediction that the energy difference between the two states increases with Δ/λ.

The evolution of the amplitude with increasing compression within the symmetric solution, as determined from the numerical solution of (4) for $M = 0$, 0.10, 0.18, is shown in Fig. 3. For $\Delta/\lambda \lesssim 0.2$, the system remains in the wrinkled state and there is very little influence of the film weight on the amplitude–compression curve. However, with $\Delta/\lambda > 0.25$, the fold amplitude increases with the film weight M, holding compression, Δ, fixed; furthermore, we recover the linear evolution of the fold amplitude with Δ. As M varies, the experimentally determined (Δ, A) curves are shifted as predicted by our theory (Fig. 3). The observed experimental fold is fully localized and downward symmetric for $\Delta/\lambda > 0.4$. Its amplitude can thus be quantitatively predicted by the numerical solution of (4) in this regime.

In fig. 3, the last point of each curve corresponds to the point at which the downward symmetric fold first self-contacts, forming a loop, *i.e.* the teardrop shape. Experimentally, we find that this point is reached for $\Delta_{sc}/\lambda \approx 0.8$ whereas using equation (4), this transition is found at a slightly higher value ($\Delta_{sc}/\lambda \approx 0.89$ for symmetric folds). The reason for this discrepancy is not immediately clear. Some insight into this shift is obtained by examining a top view of the fold (inset of Fig. 3): its shape is not the same at the edge of the film and at its centre . Capillary forces pull the elastic film on its sides closing the fold tighter at its edges than at its centre. Surface tension slightly distorts the fold's shape at the sheet's edges, which explains the small discrepancy between the theoretical and experimental Δ_{sc}. However the fold's amplitude remains constant even when subjected to surface tension effects (see ESI† for details).

3.2 Evolution of the fold

The analytical solutions (2) and the numerical solutions of (4) cease to be relevant beyond self-contact ($\Delta > \Delta_{sc}$) since, within the limitations of our model, the numerically generated profiles interpenetrate. Experimentally, we observe two different behaviours depending on the dimensionless mass M, defined in (3), as shown in Fig. 4 (a)-(f): heavy films ($M \gtrsim 0.14$) retain a symmetric configuration and encapsulate a column of the upper fluid in a teardrop shape fold (Fig. 4 (d)-(e)) that grows deeper as the compression increases (Fig. 4 (f)). Lighter films ($M \lesssim 0.14$) start symmetric with the same teardrop shape but, as the compression increases, the loop starts to tilt and grows back up towards the interface (Fig. 4 (a)-(b)) where it finally reaches an obstacle such as the clamped edges or itself (Fig. 4 (c)). To quantify these observations, we first define the amplitude after self-contact, A^*, as the depth of the centre of the loop, see the inset of Fig. 4 (g). This quantity is clearly defined beyond self-contact, while before self-contact, $A^* \equiv A$. Fig. 4 (g) shows the experimentally measured amplitude as a function of the compression before and after self-contact. We vary the film density and length and present our results using the dimensionless mass M described previously. At the scale of Fig. 4 the variation of amplitude due to the mass M is not visible before self-contact; immediately after self-contact the amplitude initially keeps growing linearly ($A^*/\lambda \approx 0.5\Delta/\lambda$). However, as the compression is increased beyond self-contact, the influence of M becomes more apparent, at a critical compression Δ_b the fold begins to tilt back up towards the interface with increasing compression *i.e.*: A^* decreases. (We emphasize that this tilting occurs quasi-statically.) Fig. 4 (g) shows that as M increases, the transition from a straight to a tilted fold occurs at larger Δ_b. Finally, when the elastic film is sufficiently dense ($M = 0.18$ in Fig. 4 (g)), the fold never bends back up and sinks indefinitely into the liquid subphase.

To understand the tilting behaviour of the loop, we first consider its properties at the point of self-contact. The key quantities of interest are the loop's width w and height h. Experiments show that these grow linearly with λ (see Fig. 5 (b)) but do not vary with compression beyond self-contact (see inset of Fig. 5 (b)). We believe that this lack of evolution of the teardrop shape is due mainly to the constant volume of the upper liquid that is trapped in the loop after the point of self-contact. The teardrop shape observed corresponds to that predicted by the solution of equations (2) and (4) *at* self-contact (Fig. 5 (a)). However, the values of w and h are slightly overestimated by the model since we can only measure the shape at the film edges, where surface tension effects come into play; at the centre of the film the loop is wider (see inset Fig. 3). The numerical solution of equation (4) predicts that the loop formed at self-contact shrinks as M increases. We were not able to observe this experimentally, and conclude that this effect must be smaller than the role of surface tension at the film edges.

We compare our results to the numerical work by Demery *et al.*[35] where they study a compressed film after self-contact; however, they do not incorporate the weight of the film itself. They find two possible configurations for the shape of the film in this case: a symmetric one (which we also observe experimentally) and an antisymmetric one (which we have never observed). In the weightless case the antisymmetric configuration has a lower energy — its energy saturates with increasing Δ, while the energy of the symmetric downward fold *increases* linearly with Δ. In our case the added weight of the film reduces the energy of the symmetric configuration by $U_g \sim -M\Delta^2$, explaining why this configuration is ultimately energetically favourable.

To describe the evolution of the fold when $\Delta > \Delta_{sc}$ in more detail, we need a new mathematical model. We continue to neglect surface tension so that the film behaviour is invariant along its width and the problem can be treated as two-dimensional. Our model of the elastic film after self-contact is illustrated schematically in Fig. 6. We break the system in two parts: a heavy beam corresponding to the part of the film in self-contact and a force F acting at its tip (which is the teardrop shape encapsulating buoyant fluid). Here

$$F = \Delta\rho g \mathscr{A} - (\rho_s - \rho_w) g t \mathscr{L}, \tag{5}$$

$\mathscr{A}$ and $\mathscr{L}$ are respectively the half-area and half the perimeter of the upper fluid encapsulated in the teardrop (see schematic in the inset of Fig. 6). Considering these half quantities means that we are considering each half of the two that are in contact separately, and assuming they do not exert force on one another. While this reduction suggests that the problem is equivalent to that of a beam subject to a constant load at one end, we

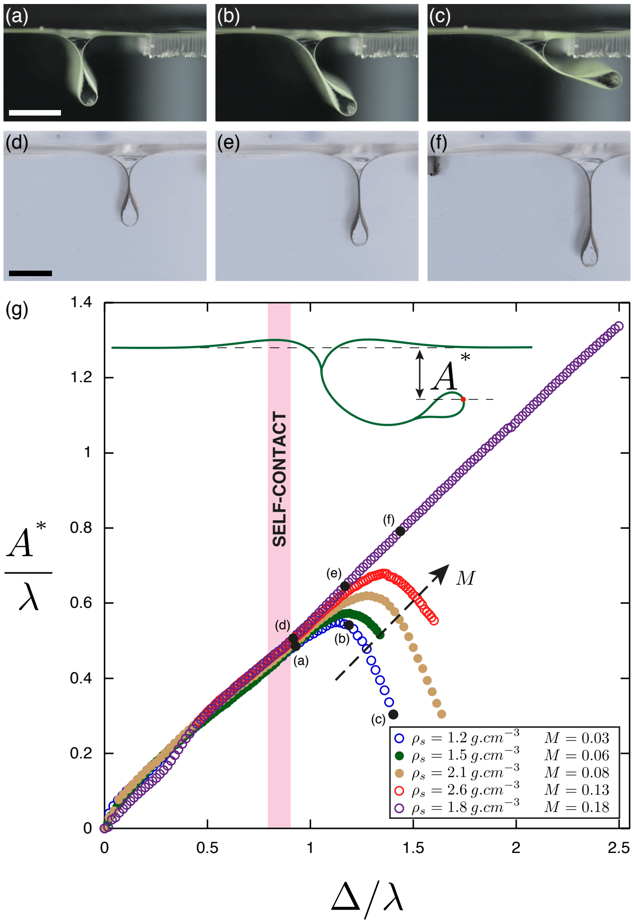

Fig. 4 Images from the side of two folds as compression is increased. The two sets of pictures have the same dimensionless compressions, from left to right $\Delta/\lambda \approx 0.93, 1.19, 1.44$. Scalebars: 5 mm. **(a)-(c)** film with a low mass $M = 0.03$, $\rho_s = 1.20$ gcm^{-3}. **(d)-(e)** film with a high mass $M = 0.18$, $\rho_s = 1.8$ gcm^{-3}. Colours have been inverted to enhance contrast. **(g)** *Inset*: Schematic presenting the post buckling fold amplitude A^* (fold centre in red). Dimensionless wrinkle/fold amplitude A^* as a function of the dimensionless compression after self-contact. (○, ○, ○) represents oil/water experiments, (●, ●) air/water experiments. ● show the data corresponding to the pictures **(a)-(f)**.

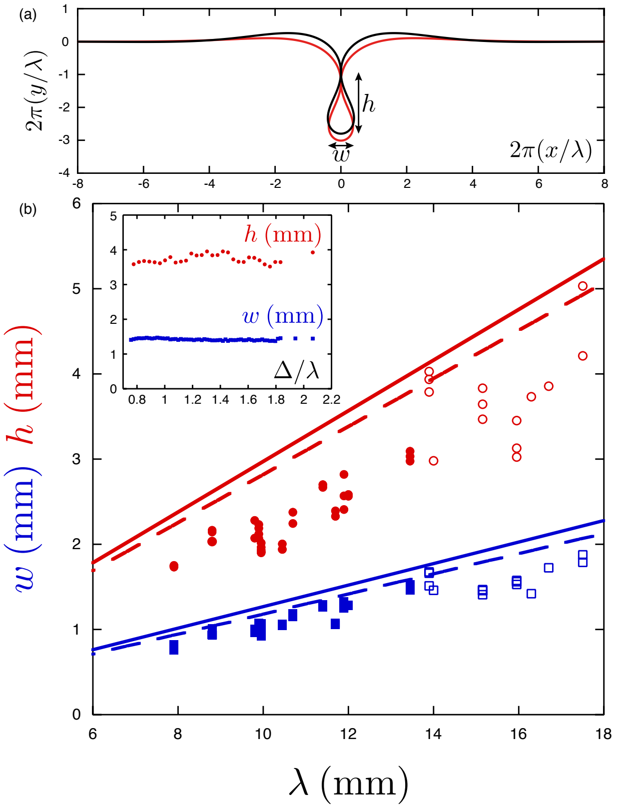

Fig. 5 **(a)** Comparison of symmetric profiles at self-contact given by the analytical solution (2) for $M = 0$ (black) and the shape for $M = 0.18$, determined from the numerical solution of equation (4) (red). The arrows define the height h and the width w of the teardrop. **(b)** The teardrop height h (red circles) and width w (blue squares) as a function of the wavelength. Closed symbols represent air/water experiments, open symbols oil/water experiments; here, solid lines correspond to the analytical prediction, based on equation (2), while dashed lines correspond to the numerical solution of equation (4) for $M = 0.18$. All other experimental parameters are found to be not relevant and vary across the data. *Inset*: Experimental teardrop height and width in one experiment ($M = 0.14$, $\rho_s = 1.8\,\mathrm{g\,cm^{-3}}$) as a function of the compression.

emphasize that the self-weight of the beam is important and so instead we must consider a ‘heavy hanging column’ [36], subject to a constant force pushing at the tip (since we have already found experimentally that the teardrop size does not evolve with further compression). We assume a clamped boundary condition at the top for simplicity (schematic Fig. 6). At each compression step the portion in self-contact L^* grows, increasing the length of the effective beam.

We introduce again intrinsic coordinates (s,θ), with s the arc-length but now θ denotes the angle between the heavy beam and the vertical axis. The (x,y) coordinates are thus rotated clockwise by 90 degrees compared to the model presented in the previous section. In this system, the equation for the heavy hanging column is given by [36,37](see ESI† for details):

$$B\partial_s^2\theta = -[F-(\rho_s-\rho_w)gts]\sin\theta$$

B is the beam bending modulus and t its thickness. ρ_s is the beam density and ρ_w the lower liquid (water) density. The boundary conditions are that the end at $s=0$ is free while that at $s=L^*$ is clamped:

$$\partial_s\theta(s=0)=0, \quad \theta(s=L^*)=0$$

The system is made dimensionless by dividing s by L^*:

$$\partial_s^2\theta + \left[\widetilde{F} - \left(\frac{L^*}{\ell_g}\right)^3 s\right]\sin\theta = 0 \tag{6}$$

$$\partial_s\theta(s=0)=0, \quad \theta(s=1)=0.$$

Here $\widetilde{F} = FL^{*2}/B$ is the dimensionless force due to the buoyancy of the teardrop and $\ell_g = (B/[(\rho_s-\rho_w)gt])^{1/3}$ is the elasto-gravitational length, which compares elastic and gravitational forces; loosely speaking the elasto-gravitational length is the length above which the film will buckle under its own weight. The elasto-gravitational length is also closely related to the parameter M, which is defined in (3) and may be written $M = (\ell_{eh}/\ell_g)^3$.

For a fixed applied force F, the beam will buckle once the length reaches a threshold value. This threshold can be determined by linearizing (6) and solving the resulting problem analytically [36] (see ESI†). This analysis yields the critical force $\widetilde{F_c}$ needed for the beam to buckle as a function of $(L^*/\ell_g)^3$, *i.e.* $\widetilde{F_c} = \frac{F_c L^{*2}}{B} = \mathrm{f}\left((L^*/\ell_g)^3\right)$. In our experiments, the control parameter is the beam length L^*, which increases with increasing compression; the force is constant, since it originates from the buoyancy of the teardrop, which is fixed during the compression. We therefore write:

$$\frac{F\ell_g^2}{B} = \left(\frac{\ell_g}{L_c^*}\right)^2 \mathrm{f}\left(\frac{L_c^*}{\ell_g}\right) \tag{7}$$

where the function $\mathrm{f}(x)$ emerges from a solvability condition, see ESI†. For a given teardrop size, and hence buoyancy force,

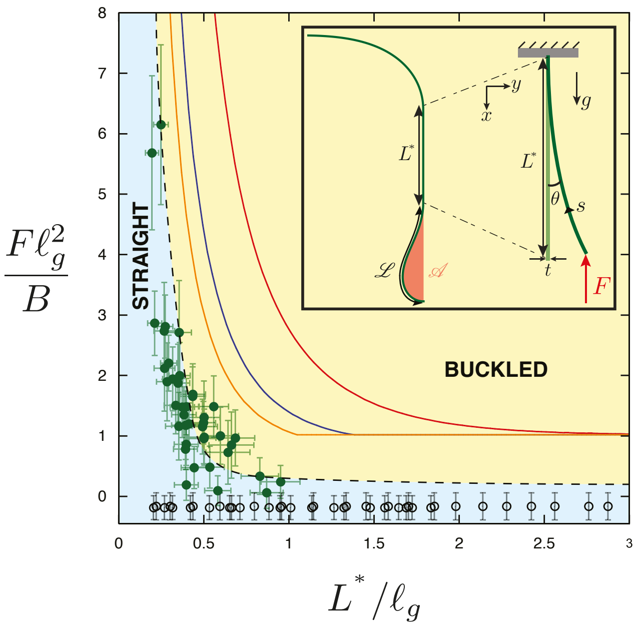

Fig. 6 Phase diagram of the post self-contact fold buckling. Green filled circles give the critical length L^* before buckling in each experiment. Black open circles represent experiments in which the fold never buckles. The black dashed curve and background colours are guides for the eye to distinguish experimental phases. The red solid curve is the analytical result of the heavy hanging column (equation (7)), the blue (respectively orange) solid curve is the numerical result of the heavy hanging column theory with an initial angle of 10° (respectively 20°). *Inset*: Schematic of a perfectly symmetric fold post self-contact. The fold is split in two parts: the portion in self-contact is treated as a heavy hanging column of length L^* and thickness t and the teardrop is modeled as a constant point force (resulting from the buoyancy of the teardrop). The upper part is not taken into account here and a clamped boundary condition is assumed at the top of the heavy hanging column. The intrinsic coordinates (s,θ) are drawn.

equation (7) may be solved to give the critical length at which the beam begins to bend.

The computed prediction for the length at which the fold should start to bend upwards is presented in Fig. 6. Here, the buoyancy force of the teardrop is calculated using equation (5) with $\mathscr{A}$, $\mathscr{L}$ and L^* measured from images taken from the side (and are hence subject to the inaccuracies discussed earlier) and B is calculated based on the measurement of the film wrinkling wavelength ($B = \Delta\rho g \left[\lambda/(2\pi)\right]^4$). This calculation, via equation (7), captures qualitatively the experimentally observed fold behaviour. In particular, there is a critical buoyancy force below which the fold never buckles, regardless of the length of the film.

The experimental data points shown in Fig. 6 lie well below the prediction of equation (7), although the trend is similar. We believe that in most experiments this discrepancy occurs because the fold is not perfectly aligned with the vertical axis when it reaches self-contact (Fig. 4(a)). The average angle α between the fold and the vertical axis is $|\alpha| = 10°$. To account for this angle, we may include this effect by changing the boundary condition at the top of the beam: $\theta(s=1) = \alpha$. We now solve the problem numerically (using equation (6)) to determine the critical length L_c^*/ℓ_g for buckling (see ESI† for details). The results are plotted in Fig. 6 (blue curve: $\alpha = 10°$, orange curve: $\alpha = 20°$) and are closer to the experimental values. An additional source of discrepancy between the experimental results and the numerical model may be, once again, that we underestimate the size of the teardrop, since we measure its shape at the edge of the film (where it is affected by surface tension) and not at its centre. It may also be due to how we oversimplify the boundary condition at the top of the beam. Here, we have assumed that a clamped boundary condition is appropriate but we have observed that the top of the fold can slide and rotate slightly as the compression is varied.

4 Conclusion

We have studied experimentally the behaviour of thin elastic films under uniaxial compression at a liquid-fluid interface. As previously observed, when confinement increases the film undergoes a transition from a uniform wrinkled state to a localized configuration in which a single fold is observed. We showed that the film weight affects the wrinkle-to-fold transition, breaking the up-down symmetry of the light film problem considered previously. More importantly, however, the film weight plays a large role in the evolution of the fold beyond the transition: it may bend back towards the fluid interface or grow deeper as compression is increased. A simple model predicts the two possible behaviours in a phase diagram.

The experimental results presented here allow us to confirm some previous theoretical assumptions but also highlight the role of the film weight and surface tension in the formation and evolution of a fold. The teardrop shape observed after self-contact seems similar to the so-called “self-encapsulation” of an elastic rod which is observed in a solely elastic situation when a rod covering a fixed span is loaded at the middle with a transverse force such that two points of the rod come into contact with each other[38]. Finally, this study could give insight into the elastic properties of compressed particle-laden interfaces, which exhibit a wrinkling instability similar to that described for elastic films in this Letter. For example, our results show that such films may encapsulate a teardrop of the upper (lower) fluid if the dimensionless parameter $M > 0$ ($M < 0$); this may provide a novel route for the creation of cylindrical, particle-coated droplets[39] by compressing a particle-laden interface. In such settings, the granular aspect of the interface allows the interface’s mechanical properties to be tuned by probing new parameters such as the particle size, density or packing fraction[40] as well as the solid-liquid contact angles. However, the granular aspect also affects the stress state within the layer at the onset of wrinkling[41] meaning that the transition from wrinkles to localized folds upon further compression remains to be carefully characterized in such systems.

5 Acknowledgement

We are grateful to Sébastien Neukirch, Vincent Démery and Claude Perdigou for useful discussions as well as Aurélie Fargette for her help with the preparation of thin films and Julien Chopin for his expertise with the tensile testing.

References

1 D. D. Pollard and R. C. Fletcher, *Fundamentals of Structural Geology*, Cambridge University Press, 2005.
2 D. C. Van Essen, *Nature*, 1997, **385**, 313–318.
3 R. Toro and Y. Burnod, *Cerebral Cortex*, 2005, **15**, 1900–1913.
4 T. Tallinen, J. Y. Chung, F. Rousseau, N. Girard, J. Lefevre and L. Mahadevan, *Nat. Phys.*, 2016, **12**, 588–593.
5 M. Kücken and A. C. Newell, *EPL (Europhysics Letters)*, 2004, **68**, 141.
6 M. Trejo, C. Douarche, V. Bailleux, C. Poulard, S. Mariot, C. Regeard and E. Raspaud, *Proc. Natl. Acad. Sci. U. S. A.*, 2013, **110**, 2011–2016.
7 J. A. Rogers, T. Someya and Y. Huang, *Science*, 2010, **327**, 1603–1607.
8 R.-H. Kim, D.-H. Kim, J. Xiao, B. H. Kim, S.-I. Park, B. Panilaitis, R. Ghaffari, J. Yao, M. Li, Z. Liu, V. Malyarchuk, D. G. Kim, A.-P. Le, R. G. Nuzzo, D. L. Kaplan, F. G. Omenetto, Y. Huang, Z. Kang and J. A. Rogers, *Nat. Materials*, 2010, **9**, 929–937.
9 N. Bowden, S. Brittain, A. G. Evans, J. W. Hutchinson and G. M. Whitesides, *Nature*, 1998, **393**, 146–149.
10 A. Schweikart and A. Fery, *Microchim. Acta*, 2009, **165**, 249–263.
11 J. B. Kim, P. Kim, N. C. Pegard, S. J. Oh, C. R. Kagan, J. W. Fleischer, H. A. Stone and Y.-L. Loo, *Nat. Photonics*, 2012, **6**, 327–332.
12 H. Lin, Y. Wang, Y. Gan, H. Hou, J. Yin and X. Jiang, *Langmuir*, 2015, **31**, 11800–11808.
13 E. Cerda and L. Mahadevan, *Phys. Rev. Lett.*, 2003, **90**, 074302.
14 B. Li, Y.-P. Cao, X.-Q. Feng and H. Gao, *Soft Matter*, 2012, **8**, 5728–5745.
15 P. Reis, F. Corson, A. Boudaoud and B. Roman, *Phys. Rev. Lett.*, 2009, **103**, 045501.
16 F. Brau, H. Vandeparre, A. Sabbah, C. Poulard, A. Boudaoud and P. Damman, *Nat. Phys.*, 2011, **7**, 56–60.
17 P. Kim, M. Abkarian and H. A. Stone, *Nat. Materials*, 2011, **10**, 952–957.
18 R. Levien, *The Elastica: A Mathematical History*, EECS Department, University of California, Berkeley technical report, 2008.
19 L. D. Landau and E. M. Lifschitz, *The Theory of Elasticity*, Pergamon, 1970.
20 L. Pocivavsek, R. Dellsy, A. Kern, S. Johnson, B. Lin, K. Y. C. Lee and E. Cerda, *Science*, 2008, **320**, 912–916.
21 D. P. Holmes and A. J. Crosby, *Phys. Rev. Lett.*, 2010, **105**, 038303.
22 H. King, R. D. Schroll, B. Davidovitch and N. Menon, *Proc. Natl. Acad. Sci. U. S. A.*, 2012, **109**, 9716–9720.
23 M. Piñeirua, N. Tanaka, B. Roman and J. Bico, *Soft Matter*, 2013, **9**, 10985.
24 B. D. Leahy, L. Pocivavsek, M. Meron, K. L. Lam, D. Salas, P. J. Viccaro, K. Y. C. Lee and B. Lin, *Phys. Rev. Lett.*, 2010, **105**, 058301.
25 W. Lu, C. Knobler, R. Bruinsma, M. Twardos and M. Dennin, *Phys. Rev. Lett.*, 2002, **89**, 146107.
26 T. Boatwright, A. J. Levine and M. Dennin, *Langmuir*, 2010, **26**, 12755–60.
27 D. Vella, P. Aussillous and L. Mahadevan, *EPL (Europhysics Letters)*, 2004, **68**, 212.
28 T. J. W. Wagner and D. Vella, *Phys. Rev. Lett.*, 2011, **107**, 044301.
29 H. Diamant and T. A. Witten, *Phys. Rev. Lett.*, 2011, **107**, 164302.
30 H. Diamant and T. A. Witten, *Phys. Rev. E*, 2013, **88**, 012401.
31 F. Brau, P. Damman, H. Diamant and T. A. Witten, *Soft Matter*, 2013, **9**, 8177–8186.
32 M. Rivetti, *C. R. Mecanique*, 2013, **341**, 333–338.
33 M. Rivetti and S. Neukirch, *J. Mech. Phys. Solids*, 2014, **69**, 143–155.
34 O. Oshri, F. Brau and H. Diamant, *Phys. Rev. E*, 2015, **91**, 052408.
35 V. Démery, B. Davidovitch and C. D. Santangelo, *Phys. Rev. E*, 2014, **90**, 042401.
36 C.-Y. Wang and B. Drachman, *J. Appl. Mech.*, 1981, **48**, 668.
37 C. Wang, *Int. J. Mech. Sci.*, 1986, **28**, 549 – 559.
38 F. Bosi, D. Misseroni, F. Dal Corso and D. Bigoni, *Proc. R. Soc. A*, 2015, **471**, 20150195.
39 A. B. Subramaniam, M. Abkarian, L. Mahadevan and H. A. Stone, *Nature*, 2005, **438**, 930–930.
40 P. Petit, A.-L. Biance, E. Lorenceau and C. Planchette, *Physical Review E*, 2016, **93**, 042802.
41 P. Cicuta and D. Vella, *Physical Review Letters*, 2009, **102**, 138302.